coatings

MDPI

Article

Cylinder Fatigue Design of Low-Speed, High-Torque Radial Piston Motor

Lifu Cheng *, Xinyuan Chen and Guoqian Wei

Key Laboratory of Metallurgical Equipment and Control Technology, Wuhan University of Science and Technology, Ministry of Education, Wuhan 430081, China

* Correspondence: chenglifu@wust.edu.cn; Tel.: +86-137-2024-9802

Abstract: Through the comparison of fatigue properties of components made of composite materials and high-strength structural steel materials, this study proves that composite materials can replace traditional steel materials used in the production of mechanical structural components. The focus of this study was a low-speed, high-torque radial piston motor mounted on a roadheader. According to different theories, the motor block was designed using a composite material made of carbon fiber, a classic high-strength structural steel, and an aluminum alloy. The thickness of the motor cylinder obtained by theoretical calculation was verified by finite-element numerical simulation technology, and the fatigue phenomenon caused by the time change of the piston cylinder pressure was considered. The results showed that the stress results of the numerical simulation verify the rationality of the theoretical calculation of the cylinder size. In terms of safety factors, the motor cylinder made of composite materials was close to the motor cylinder made of high-strength structural steel, and the difference between the static safety factor and fatigue safety factor was only 0.8 and 0.86. The weight of the motor cylinder made of composite material was reduced from 32 N to 7 N compared with steel material, which was about 78% lighter. This is of great significance for improving the use efficiency of equipment and reducing fuel costs.

Keywords: hydraulic motor cylinder; composite material; finite-element analysis; fatigue analysis; lightweight

check for updates

Citation: Cheng, L.; Chen, X.; Wei, G. Cylinder Fatigue Design of Low-Speed, High-Torque Radial Piston Motor. *Coatings* **2022**, *12*, 1192. https://doi.org/10.3390/coatings12081192

Academic Editors: Filippo Berto and Giorgos Skordaris

Received: 29 June 2022
Accepted: 12 August 2022
Published: 16 August 2022

Publisher's Note: MDPI stays neutral with regard to jurisdictional claims in published maps and institutional affiliations.

Copyright: © 2022 by the authors. Licensee MDPI, Basel, Switzerland. This article is an open access article distributed under the terms and conditions of the Creative Commons Attribution (CC BY) license (https://creativecommons.org/licenses/by/4.0/).

1. Introduction

With economic development, there is a huge global demand for transportation and mining of mineral resources [1,2].To meet these demands, construction machinery plays an important role [3,4]. These large equipment bodies are prone to fatigue after long-term service, causing damage to parts, especially some transmission parts in the equipment body [5,6]. For example, in the low-speed, high-torque hydraulic motor in the second transport mechanism of the roadheader, the motor cylinder is easily damaged by fatigue and needs to be designed to account to mitigate this. The step-response characteristics of the motor and the dynamic relationship between the rotational speed, torque, power output, and volume flow have been deeply studied [7,8]. With the improvement in human living standards, protecting the environment is a key consideration in product design and manufacturing [9,10]. The design of structural components should take into account the production process of the material and select materials that produce less pollution [11,12]. Over the years, we have invested heavily in solutions related to electrification in order to improve the efficiency of machinery and equipment [13,14], and we have also made great efforts to improve the performance of engines [15]. To reduce carbon dioxide emissions, new and high-performance materials are used to operate on these mechanical components [16,17]. For example, parts are made of composite materials, aluminum alloys, or plastic-rubber materials, which can greatly improve machine performance and reduce production costs [18–20].

Composite materials are very advantageous for structural components because of their excellent mechanical properties and markedly low density [21,22], and for these reasons they have applications in other fields besides construction machinery [23,24]. The use of these materials can reduce the inertia and acceleration of components, which are very important factors for high-frequency applications in the field of construction machinery [25,26]. Research has shown that composites have advantages in large system components, especially where lighter and more compact systems are required [27]. Some scholars only analyze parts under static load conditions, but under actual operating conditions, many components experience fatigue, leading to component fracture failure.

The purpose of this study was to compare the fatigue resistance of structural components made of composites with conventional metal components in a low-speed, high-torque radial piston motor cylinder block mounted on a roadheader. These components are subjected to successive low and high pressure phases, which act to induce cyclic stress. In this paper, the fatigue behavior of composite materials and commonly used traditional metal materials under cyclic loading was investigated. Different materials were used in this study: high-strength structural steel (42CrMo), which is generally the most commonly used, aluminum alloy Al7075-T6, and a composite material made of epoxy resin and carbon fiber. First, dimensional problems were analyzed using appropriate theories for different materials, using three theories of composite materials: membrane stress theory, carpet plot, and winding-angle method. Second, the specific structure of the assembly was designed and a 3D model built. Finally, through finite-element numerical simulation, the calculation results of 3D models of different materials were analyzed to verify the rationality of the theoretical results, and the safety factor and weight of different materials were evaluated and compared under static and fatigue conditions. It is proposed that the composite parts replace the traditional metal parts under the condition that the fatigue life was guaranteed to be equivalent. This is of great significance for reducing the quality of the assembly, improving the mechanical efficiency, reducing the amount of metal used, protecting the environment, and reducing the emission of harmful gases.

2. Materials and Methods

2.1. Motor Cylinder Parameters

The object of this study was a low-speed, high-torque radial piston motor, which is installed on the first transport mechanism of the roadheader, as shown in Figure 1.

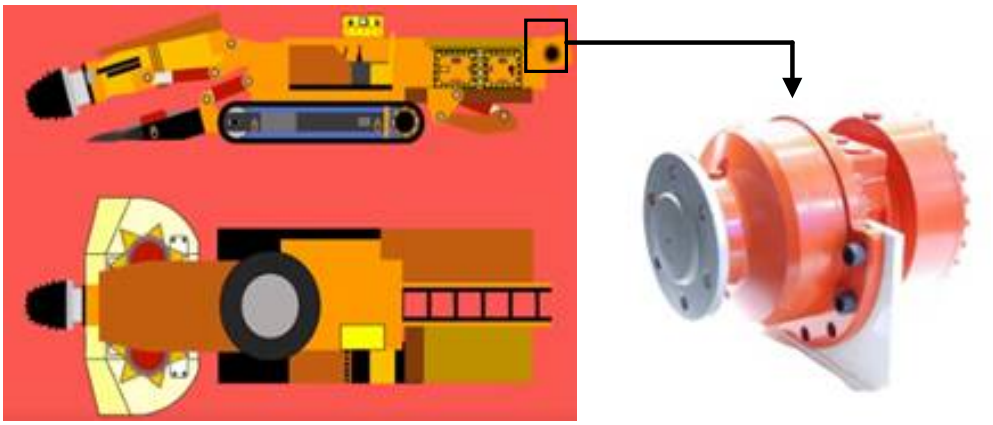


Figure 1. Low-speed, high-torque radial piston motor on a roadheader.

Under the action of hydraulic oil force, the motor pushes the piston to reciprocate in the cylinder to realize the continuous rotation of the cylinder. The motor components are shown in Figure 2 and Table 1.

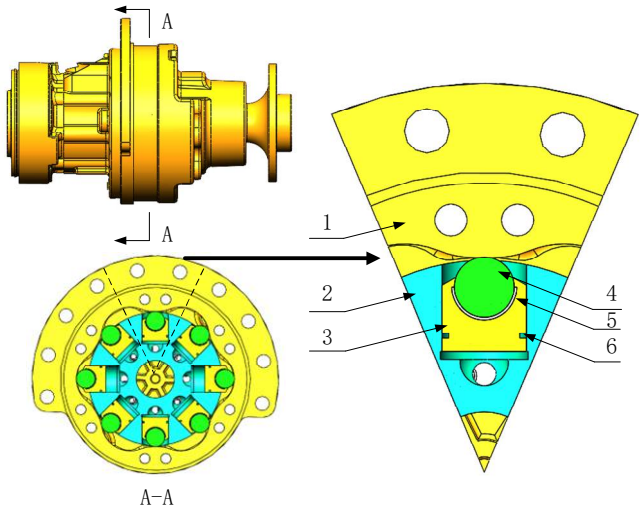


Figure 2. Motor components.

Table 1. The main components of the motor are shown in Figure 2.

Serial Number	1	2	3	4	5	6
Part name	Stator	Cylinder	Piston	Roller	Tile	Piston ring

The motor performance and the dimensions of the cylinder block are shown in Tables 2 and 3.

Table 2. Motor parameters.

Motor Power P [kw]	Quality m [kg]	Displacement q [mL/r]	Preset Pressure P [MPa]	Rated Torque T [N·m]	Rated Speed n [r/min]
25	55	468	30	1749	90

Table 3. Cylinder size.

Cylinder Diameter D [mm]	Cylinder Bore Diameter d [mm]	Number of Cylinders N
163	33.3	8

With regard to the load, it is necessary to calculate the size of the inner cavity pressure when the motor cylinder is working. The load conditions acting in the cylinder can be defined, and the pressure in the cylinder can be calculated by Equation (1), assuming the motor is subject to the maximum load [28]:

$$P = \frac{F}{A_0} \tag{1}$$

where P is the pressure in the cylinder, A_0 is the area of the bottom surface of the piston, and F is the thrust that the piston bears. The internal pressure of the cylinder barrel is different when oil is sucked and discharged, and the pressure inside the cylinder barrel is relatively large when oil is sucked. From a safety point of view, it is assumed that P = 30 MPa.

In terms of material selection, typically these parts are made of structural steel 42CrMo, but this material is obviously much denser than composites. Composites have good mechanical properties and very low density, properties that can lead to significant weight savings. In the specific case of this paper, the selection ratio of carbon fiber and epoxy

resin composite materials was 60% and 40%, respectively. In addition to these two material options, it was decided to go with the aluminum alloy Al7075-T6. Aluminum alloy is a material with high performance in terms of structural parts and low density, which ensures weight savings. Tables 4–6 show the properties of the employed materials [29–31].

Table 4. Main properties of steel and aluminum used in the cylinder block.

Material	Density ρ [kg/m^3]	Young's Modulus E [MPa]	Poisson's Ratio ν	Yield Strength σ_s [MPa]	Tensile Strength σ_b [MPa]
42CrMo	7850	212,000	0.28	950	1100
Al 7075-T6	2800	72,000	0.33	450	560

Table 5. Composite properties.

Material	Density ρ [kg/m^3]	Young's Modulus E [MPa]	Shear Modulus G [MPa]	Poisson's Ratio ν	Fiber Volume [%]
Epoxy resin	1200	2800	1600	0.4	40
Carbon fiber	1750	230,000	50,000	0.3	60

Table 6. Mechanical properties according to fiber orientation.

Material	Density ρ [kg/m^3]	Young's Modulus E_x [MPa]	Young's Modulus E_y [MPa]	Shear Modulus G_{xy} [MPa]	Main Poisson's Ratio ν_{xy}	Sub-Poisson's Ratio ν_{yx}
Composite material	1530	134,000	7000	4200	0.25	0.013

Finally, composite properties in the plane of the laminate are shown in Figure 3. In most cases, stress and deformation studies in these materials were reduced to 1–2 plane studies [32]. Table 7 mentions these properties [33].

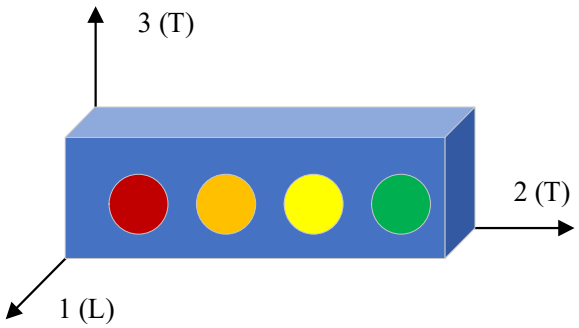


Figure 3. Laminate reference system.

Table 7. Laminate mechanical properties.

Material	X_{1T} [MPa]	X_{1C} [Mpa]	Y_{2T} [Mpa]	Y_{2C} [Mpa]	S_{12} [Mpa]
Composite material	1270	−1130	42	−141	63

2.2. Three Theories of Cylinder Design

Considering the motor cylinder as a thin-walled pressure vessel, the dimensions of the structural steel motor cylinder were calculated. For this reason, we can use the known theory of isotropic materials and the load conditions under which the motor operates, and after evaluating the stress acting in the cylinder, we can obtain the minimum thickness

of the cylinder barrel. The pressure vessel design code recommends using the minimum allowable stress, as shown in Equation (2) [34]:

$$\sigma_{adm} = min\left(\frac{R_{eH}}{1.5}; \frac{R_m}{2.4}\right) \quad (2)$$

where σ_{adm} is the allowable stress, R_{eH} is the upper yield strength, and R_m is the tensile strength. Table 8 shows these values for steel and aluminum materials.

Table 8. Allowable stresses for steel and aluminum.

Material	σ_{adm} [MPa]
42CrMo	458
Al 7075-T6	233

For the minimum thickness of the cylinder, this paper defines it as the minimum distance from the section of the cylinder to the surface of the cylinder. To determine the minimum thickness of the cylinder, Equation (3) can be used on hydraulic components. The theory is based on the Guest–Tresca maximum stress criterion, which is applied to the calculation of the minimum thickness of the cylinder, and the maximum stress is shown in Equation (3) [34]:

$$\sigma^*_{G-T} = \frac{p \cdot d}{2 \cdot S} + p \quad (3)$$

where σ^*_{G-T} is the maximum stress of the cylinder, P is the inner pressure of the cylinder, d is the inner diameter of the cylinder, and S is the minimum thickness of the cylinder. Taking the maximum stress of the cylinder as the allowable stress of the material, the minimum thickness S of the cylinder can be deduced, as shown in Equation (4) [28].

$$s = \frac{p \cdot d}{2(\sigma_{adm} - p)} \quad (4)$$

There are three different methods for sizing cylinder composites based on three different common theories. Using membrane stress theory, calculate the main dimensions of the cylinder, including the calculation process for the determination and verification of the thickness of the laminate, using the composite laminate type and loading conditions as starting data. Since the thin-wall theory is adopted, bending effects are not considered [35]. The thickness of the cylinder laminate can be further calculated according to the allowable stress. To facilitate the study, the layer plane was chosen to match the principal coordinate system (circumferential and axial) of the pressure vessel. Shearing effects do not occur and the circumferential stress is directed to the longitudinal axis of the ply, while the axial stress is transverse, and the isotropic stress can be obtained as Equations (5)–(7) [34]:

$$N_x(\sigma_\theta) = \frac{p \cdot d}{2 \cdot s} \quad (5)$$

$$N_y(\sigma_z) = \frac{p \cdot d}{4 \cdot s} \quad (6)$$

$$N_{xy} = 0 \quad (7)$$

where $N_x(\sigma_\theta)$, $N_y(\sigma_z)$, and N_{xy} are the circumferential stress, axial stress, and shear stress, respectively. Figure 4 shows the adopted coordinate system [36].

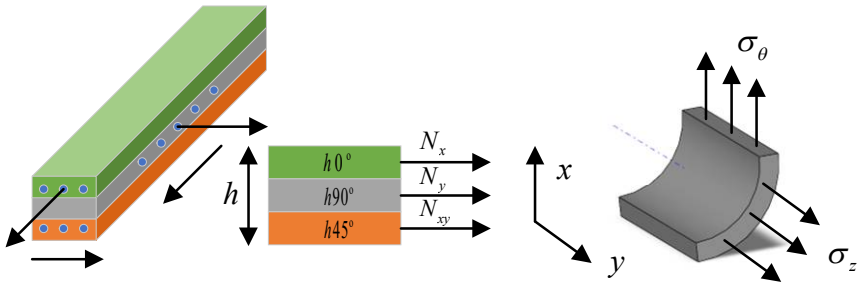


Figure 4. Laminate and cylinder reference system.

Divide the resulting membrane stress by the maximum resistance of the material in the different directions by the corresponding thickness, as shown in Equations (8)–(10) [28]:

$$h_{0^\circ} = h_x = \frac{N_x}{\sigma^{0^\circ}_{x-max}} \tag{8}$$

$$h_{90^\circ} = h_y = \frac{N_y}{\sigma^{90^\circ}_{y-max}} \tag{9}$$

$$h_{\pm 45^\circ} = h_{xy} = \frac{N_{xy}}{\tau^{\pm 45^\circ}_{xy-max}} \tag{10}$$

where h_{0°, h_{90°, and $h_{\pm 45^\circ}$ are the thicknesses in the 0°, 90°, and ±45° directions, respectively, h_x, h_y, and h_{xy} are the thicknesses in the x, y, and xy directions, respectively, $\sigma^{0^\circ}_{x-max}$, $\sigma^{90^\circ}_{y-max}$, and $\tau^{\pm 45^\circ}_{xy-max}$ are the maximum stress in the x direction, y direction. and xy direction, respectively.

Now, the ratio of the reference layer thickness to the total thickness can be determined, as shown in Equations (11)–(13) [28]:

$$p^{0^\circ} = \frac{h_x}{h_x + h_y + h_{xy}} \tag{11}$$

$$p^{90^\circ} = \frac{h_y}{h_x + h_y + h_{xy}} \tag{12}$$

$$p^{\pm 45^\circ} = \frac{h_{xy}}{h_x + h_y + h_{xy}} \tag{13}$$

where P^{0°, P^{90°, and $P^{\pm 45^\circ}$ are the ratios of the thickness of the x direction, the y direction, and the xy direction to the total thickness, respectively.

Continuing to verify the obtained results, it is generally necessary to verify whether the calculated thickness can withstand the stresses experienced by the laminate. In order to calculate these stresses, the relevant material parameters need to be obtained [34], or rather, those elastic characteristics that assimilate the laminate behavior (the object of this study) into orthotropic laminates. Using them, the midplane laminate strain can be calculated with zero bending strain. The matrix that allows the correlation between strain values and stresses in the laminate (not the individual layers) is shown in Equation (14) [37,38]. The terms indicated by the overscores refer to the properties of the laminate:

$$\begin{bmatrix} \varepsilon^0_x \\ \varepsilon^0_y \\ \gamma^0_{xy} \end{bmatrix} = \begin{bmatrix} \frac{1}{\overline{E_x}} & -\frac{\overline{\nu_{yx}}}{\overline{E_y}} & 0 \\ -\frac{\overline{\nu_{xy}}}{\overline{E_x}} & \frac{1}{\overline{E_y}} & 0 \\ 0 & 0 & \frac{1}{\overline{G_{xy}}} \end{bmatrix} \begin{bmatrix} \sigma^0_x \\ \sigma^0_y \\ \tau^0_{xy} \end{bmatrix} \tag{14}$$

where ε_x^0, ε_y^0, and γ_{xy}^0 represent the strains in the x direction, y direction, and xy direction of the midplane of the laminate, the magnitude depends on the thickness of the laminate, E_x, E_y, $\overline{v_{xy}}$, $\overline{v_{yx}}$, and $\overline{G_{xy}}$ are the material constants, and σ_x^0, σ_y^0, and τ_{xy}^0 represent the layers stresses in the x, y, and xy directions in the midplane of the plywood. These values are calculated as shown in Equation (15) [37]:

$$\begin{bmatrix} \sigma_x^0 \\ \sigma_y^0 \\ \tau_{xy}^0 \end{bmatrix} = \begin{bmatrix} N_x/h \\ N_y/h \\ N_{xy}/h \end{bmatrix} \tag{15}$$

where h is the calculated thickness of the first laminate. Note that the deformation and stress in the midplane are the same for all layers. One of the things that will change is the stress values between the orientations of the laminate layers. In order to calculate them, the stiffness matrix in each direction is required, and the different layer stresses are calculated, as shown in Equation (16) [37]:

$$\begin{bmatrix} \sigma_x \\ \sigma_y \\ \tau_{xy} \end{bmatrix}_k = \begin{bmatrix} \overline{Q_{11}} & \overline{Q_{12}} & \overline{Q_{16}} \\ \overline{Q_{12}} & \overline{Q_{22}} & \overline{Q_{26}} \\ \overline{Q_{16}} & \overline{Q_{26}} & \overline{Q_{66}} \end{bmatrix} \begin{bmatrix} \varepsilon_x \\ \varepsilon_y \\ \gamma_{xy} \end{bmatrix}_k \tag{16}$$

where k represents the layer direction, σ_x, σ_y, and σ_{xy} are the stresses in the x, y, and xy directions of the layer, respectively, and ε_x, ε_y, and γ_{xy} are the strains in the x, y, and xy directions of the layer, respectively, $\overline{Q_{11}} = \frac{E_x}{1-v_{xy}v_{yx}}$, $\overline{Q_{12}} = \frac{v_{yx}E_x}{1-v_{xy}v_{yx}}$, $\overline{Q_{16}} = 0$, $\overline{Q_{12}} = \frac{v_{xy}E_y}{1-v_{xy}v_{yx}}$, $\overline{Q_{22}} = \frac{E_y}{1-v_{xy}v_{yx}}$, $\overline{Q_{26}} = 0$, $\overline{Q_{16}} = 0$, $\overline{Q_{26}} = 0$, $\overline{Q_{66}} = G_{xy}$.

When some fiber directions are different from the 0° direction, a matrix transformation is required, such as moving to the layer coordinate system, as shown in Equation (17) [34]:

$$\begin{bmatrix} \sigma_1 \\ \sigma_2 \\ \tau_{12} \end{bmatrix}_k = \begin{bmatrix} c^2 & s^2 & 2cs \\ s^2 & c^2 & -2cs \\ -sc & sc & c^2 - s^2 \end{bmatrix} \begin{bmatrix} \sigma_x \\ \sigma_y \\ \tau_{xy} \end{bmatrix}_k \tag{17}$$

where σ_1, σ_2, and τ_{12} are the stresses in the main direction, and $c = \cos\alpha$, $s = \sin\alpha$, and α are the angles between the fiber layer direction and the 0° fiber layer direction.

Now, for each orientation, the strength of the laminate is verified using the Tsai–Hill criterion, as shown in Equation (18) [39]:

$$\left(\frac{\sigma_{1k}}{X}\right)^2 + \left(\frac{\sigma_{2k}}{Y}\right)^2 - \frac{\sigma_{1k} \cdot \sigma_{2k}}{X^2} + \left(\frac{\tau_{12k}}{S}\right)^2 < 1 \tag{18}$$

where X and Y are the axial strengths in the two principal directions and S is the shear strength in the 1–2 plane. If the standard is not met, the thickness needs to be modified to get the correct result. Calculation software can be used to solve this, e.g., joint calculation in Excel and Matlab.

The second is the use of a carpet plot for sizing, including the use of tables in the literature to determine the optimal composition of laminates [35,36]. To achieve this goal, it is necessary to calculate the scale of the layers in different directions. From the previously calculated membrane stresses and applying certain relationships, the desired ratios are obtained, as shown in Equations (19)–(21) [28]:

$$\overline{N_x} = \frac{N_x}{|N_x| + |N_y| + |N_{xy}|} \tag{19}$$

$$\overline{N_y} = \frac{N_y}{|N_x| + |N_y| + |N_{xy}|} \tag{20}$$

$$\overline{N_{xy}} = 1 - \overline{N_x} - \overline{N_y} \tag{21}$$

where $\overline{N}_x$, $\overline{N}_y$, and $\overline{N}_{xy}$ are the proportion of the thickness in the 0°, 90°, and ±45° directions to the total thickness, respectively. On this basis, also knowing the ratio of fibers and matrix, using the carpet plot [36], the optimal composition of the laminate and its minimum thickness can be obtained.

The third is the winding-angle method. The results obtained by this method have nothing to do with the form of the composite material layer, but have a greater relationship with the orientation of the fibers [40]. The third method is similar to the production technique for axisymmetric parts made of composite materials [41,42]. The theory is based on the following assumptions [43]: (a) on the surface of the part, the fibers are wound along alternating angles (±α); (b) equal stress in the fiber direction. In order to calculate the optimal winding angle, a coordinate change is required. Figure 5 shows the coordinate system used and the orientation of the fibers.

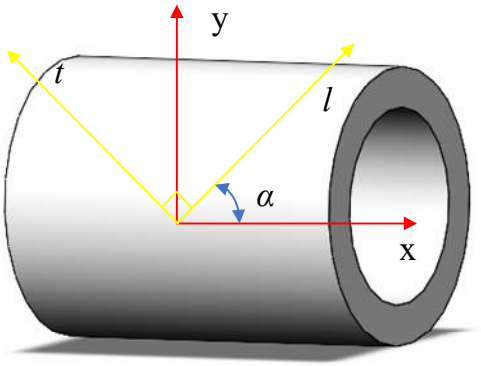


Figure 5. Primary reference frame x-y on axisymmetric parts, fiber direction l, tilt angle α and fiber normal direction t.

Rotation can be performed by a matrix, as shown in Equation (22). Through matrix transformation, the principal stress in the xy plane can be obtained, as shown in Equation (23) [34]:

$$T = \begin{bmatrix} \cos(\alpha)^2 & \sin(\alpha)^2 & 2\sin(\alpha)\cos(\alpha) \\ \sin(\alpha)^2 & \cos(\alpha)^2 & -2\sin(\alpha)\cos(\alpha) \\ -\sin(\alpha)\cos(\alpha) & \sin(\alpha)\cos(\alpha) & \cos(\alpha)^2 - \sin(\alpha)^2 \end{bmatrix} \quad (22)$$

$$\begin{bmatrix} \sigma_x \\ \sigma_y \\ \tau_{xy} \end{bmatrix} = [T]^{-1} \begin{bmatrix} \sigma_l \\ \sigma_t \\ \tau_{lt} \end{bmatrix} \quad (23)$$

where σ_x, σ_y, and τ_{xy} are the stresses in the x, y, and xy directions, T is the transformation matrix, σ_l is the stress along the fiber direction, σ_t is the stress perpendicular to the fiber direction, and τ_{lt} is the shear stress in the lt direction. Since the stress is only in the fiber direction and the shear stress is zero, τ_{lt} is equal to zero. Referring to Figure 6, the axial stress (σ_z) and circumferential stress (σ_θ) can be obtained, as shown in Equations (24) and (25). Through conversion, the stress is expressed by pressure, diameter, and thickness, and the relationship between the thickness and the stress in the fiber direction can be obtained, as shown in Equations (26) and (27) [34].

$$\sigma_x(\sigma_z) = \sigma_l \cos^2 \alpha \quad (24)$$

$$\sigma_y(\sigma_\theta) = \sigma_l \sin^2 \alpha \quad (25)$$

$$\frac{p \cdot d}{4 \cdot s} = \sigma_l \cos^2 \alpha \quad (26)$$

$$\frac{p \cdot d}{2 \cdot s} = \sigma_l \sin^2 \alpha \quad (27)$$

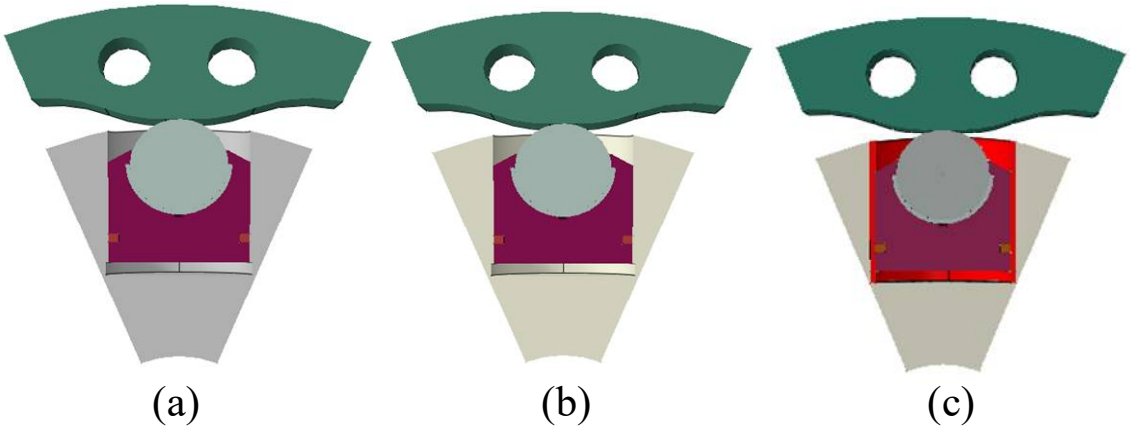


Figure 6. (**a**) Steel, (**b**) aluminum, and (**c**) composite cylinder motor assembly models.

Now, separating the σ_l term from Equation (25) or Equation (26), substituting it into Equation (27) or Equation (28), respectively, the optimal angle can be obtained. Then, use Equation (27) or Equation (28) to calculate the minimum thickness. The minimum cylinder thickness is related to the percentage of fibers present in the composite. Because the fiber accounts for 60% of the volume, the minimum thickness value needs to be multiplied by 1.6 [36,44].

2.3. Fatigue Performance Verification Theory

In order to verify the fatigue performance of the cylinder, the *S-N* curve of the composite material needs to be known. Composites made of epoxy matrix (40%) and carbon fiber (60%) have σ-*N* values related to the stress ratio, and these values are shown in Table 9 [45,46].

Table 9. For selected composites, cyclic alternating stress, stress ratio R = 0.1.

Cycles	Alternating Stress [MPa]
1	780
10	770
10^2	720
10^3	650
10^4	580
10^5	530
10^6	480
10^7	430

The theoretical calculation results need to be verified according to the material fatigue behavior and the corresponding σ-N curve [47,48]. This validation is determined by the number of cycles and a factor of safety expressed by stress and applies to both composite and noncomposite materials [45]. σ-N curve can be described by a line in a logarithmic graph [49]. The relationship describing this line is shown in Equation (28) [50]:

$$\sigma \cdot N^{\mathrm{k}} = \mathrm{C} \tag{28}$$

where σ is the fatigue stress value, N is the fatigue life, and k and C are constants. At two points on the line, given the number of loops, the constants k and C can be derived. For example, 10^3 and 10^6 data points can be used. The double logarithmic relationship is shown in Equation (29) [50].

$$log\sigma = -klogN + logC \tag{29}$$

It is important in product design to generally calculate the number of cycles of a part when it is subjected to the same stress as calculated by the winding-angle method [46]. The number of allowed calculation cycles is shown in Equation (30) [50].

$$N = \left(\frac{C}{\sigma_N}\right)^{\frac{1}{k}} \tag{30}$$

We now evaluate the safety factors resulting from these conditions, including the safety factors for stress and number of cycles, as shown in Equations (31) and (32) [51]:

$$\eta_\sigma = \frac{\sigma_e}{\sigma_w} \tag{31}$$

$$\eta_N = (\eta_\sigma)^{\frac{1}{k}} \tag{32}$$

where η_σ is the stress safety factor, η_N is the cycle number safety factor under the corresponding cycle number, σ_t is the test stress, and σ_w is the design working stress.

3. Results and Discussion

Under different theories, the thickness values of the motor cylinder were designed as shown in Table 10. Due to the different emphases of each theory, the cylinder thickness calculated according to different theories was slightly different, and the overall calculation results were within a small range, which shows that the calculated cylinder thickness results in this paper were reasonable. The fatigue analysis was carried out with reference to the results under the winding-angle theory, which is a classic theory for constructing axisymmetric parts. Therefore, the cylinder thickness of 2.5 mm was adopted for the fatigue analysis, and the safety factor was assumed to be equal to 2.5 [52,53].

Table 10. Cylinder thickness estimated from three theories.

Theory Used	Calculate Thickness [mm]
Macromechanics of orthotropic layers	3.44
Carpet plot	1.17
Winding angle	0.95

Through the theoretical calculation of the thickness of the cylinder, the three-dimensional model of the cylinder of steel, aluminum, and composite materials can be established, and the assembly model of the main components of the motor can be further established for finite-element analysis. Since the eight cylinders of the motor were the same, in order to save the calculation cost, only one motor cylinder model was established in this paper. For comparative analysis, three material models were established, as shown in Figure 6.

Import the 3D model in SolidWorks modeling software into Abaqus finite-element analysis software. The mesh type adopts solid elements. In order to ensure faster convergence of the calculation process, regular hexahedral elements were mainly used, and regular tetrahedral elements were used for very irregular models. In order to better converge the model calculation, a small displacement load was firstly applied during loading, and then the load was withdrawn after the rollers and the stator were in full contact, and a compressive load was applied at the same time. The total number of nodes was 97,743, and the total number of elements was 316,419. A static analysis of the assembly model was performed and the results provided according to the Von Mises criterion. The stress results are shown in Figure 7.

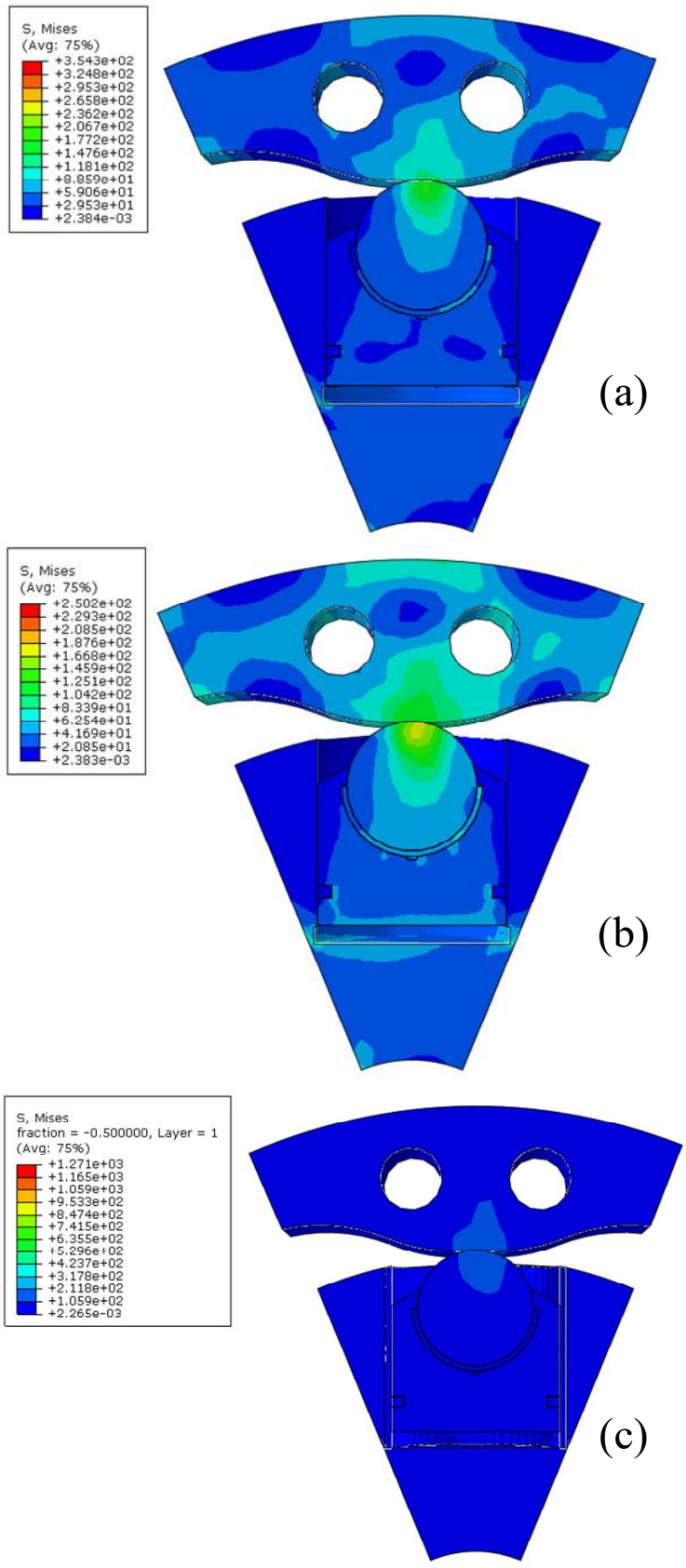


Figure 7. (**a**) Steel, (**b**) aluminum, and (**c**) composite cylinder stress cloud diagram.

From the simulation data results, it can be found that the stress on the motor cylinder is less than the yield stress of the material, which shows that the cylinder designed according to the motor cylinder design method proposed in this paper was reasonable. It can be seen from the stress cloud diagram in Figure 7 that the size obtained by the numerical simulation verification analysis and calculation can meet the working conditions. Table 11 shows the results obtained with different materials selected, where S is the thickness of the cylinder.

Table 11. Calculated cylinder thickness.

Material	S (mm)
42CrMo	1.2
Al 7075-T6	2.5
Composite material	2.5

Once the part geometry that minimizes weight is defined, its fatigue performance can be verified [54,55]. The motor cylinder object of this study was subjected to continuous pressure changes during the working phase. These pressure changes involved non-constant stresses, thus causing fatigue stress in the cylinder bore. The cylinder was subjected to 10,000 cycles, and the ratio of maximum pressure to minimum pressure was 0.1. When the cylinder block did not absorb hydraulic oil, it needed some low-pressure fluid inside the cylinder barrel—3 MPa [56]. To sum up, the data stress ratio R required for the calculation is 0.1, the number of cycles N is 10,000, and the pressure P is 30 MPa. From the data in Table 12, k = 0.044 and C = 880 [MPa] can be obtained. The working stress σ_w = 438 [MPa] and $\sigma_w = \sigma_l$ calculated by the winding-angle method and the number of resistance cycles $N = 7.7 \times 10^6$ [cycles] can be obtained.

Table 12. Cycle times and relative stress.

N	σ_N
10^3	650
10^6	480

Under the operating conditions of the cylinder under 10^4 cycles, we now evaluate the safety factor resulting from these conditions. According to the design working conditions, σ_w = 438 [MPa] and $N_w = 10^4$ [cycles]. As well as the test values σ_e = 580 [MPa] and $N_e = 10^4$ [cycles] in Table 9, the safety factor for stress and number of cycles can be obtained, and the results are shown in Table 13.

Table 13. Safety factors of composite cylinders.

η_σ	η_N
1.32	550

The results obtained show that the studied components are resistant to fatigue phenomena under the conditions analyzed. The cylinder block of composite material can reduce the mass, and can meet the needs of the work, involving pressure changes over time. Through calculation, the safety factor of different materials in terms of stress for static and fatigue phenomena can be obtained, as shown in Table 14.

Table 14. Comparison of safety factors for steel and composite cylinders.

Material	Cylinder Weight [N]	η_{static}	$\eta_{fatigue}$
42CrMo	32	2.1	2.18
Composite material	7	2.9	1.32

Comparing the traditional high-strength structural steel material with the composite material cylinder, the static safety factor and fatigue safety factor are basically the same. This shows that the motor cylinder block of composite materials can meet the working requirements in terms of the safety factor. This paper did not consider wear, but verifies that the fatigue design method of the composite motor cylinder block proposed is of great significance. Some traditional metal parts can be replaced by composite materials, thereby reducing the use of materials with higher density, effectively reducing the weight of parts and improving the performance of the equipment body.

4. Conclusions

In this paper, a reasonable hydraulic motor cylinder was designed through a series of theoretical and numerical simulations that not only prove that the composite material significantly reduces the weight of the cylinder, but more importantly, demonstrate that composite cylinders can meet fatigue life requirements. Using actual operating conditions, a specific hydraulic motor cylinder block made of three different materials was investigated. The stress results of the numerical simulation verified the rationality of the theoretical calculation of the cylinder size. The hydraulic motor cylinder designed with composite materials has little difference in static performance, especially fatigue performance, compared with traditional metal materials. This has a lot to do with the intrinsic structure of the composite material. Considering the cylinder block made of composite material and aluminum alloy, compared with the same steel cylinder block, the weight of the composite material was reduced by about 78%, and the low density of composite materials was beneficial for reducing the weight of components.

Author Contributions: Conceptualization, L.C. and X.C.; methodology, L.C. and X.C.; formal analysis, L.C. and G.W.; writing—original draft preparation, L.C.; writing—review and editing, X.C.; supervision, X.C. and G.W. All authors have read and agreed to the published version of the manuscript.

Funding: This research was funded by the National Natural Science Foundation of China (51575408).

Institutional Review Board Statement: Not applicable.

Informed Consent Statement: Not applicable.

Data Availability Statement: Not applicable.

Conflicts of Interest: The authors declare no conflict of interest.

References

1. Li, P.; Cai, M. Challenges and new insights for exploitation of deep underground metal mineral resources. *Trans. Nonferr. Met. Soc. China* **2021**, *31*, 3478–3505. [CrossRef]
2. Ağbulut, Ü. Forecasting of transportation-related energy demand and CO_2 emissions in Turkey with different machine learning algorithms. *Sustain. Prod. Consum.* **2022**, *29*, 141–157. [CrossRef]
3. Lin, T.; Lin, Y.; Ren, H.; Chen, H.; Chen, Q.; Li, Z. Development and key technologies of pure electric construction machinery. *Renew. Sustain. Energy Rev.* **2020**, *132*, 110080. [CrossRef]
4. Trinh, H.A.; Truong, H.V.A.; Do, T.C.; Nguyen, M.H.; Phan, V.D.; Ahn, K.K. Optimization-based energy management strategies for hybrid construction machinery: A review. *Energy Rep.* **2022**, *8*, 6035–6057. [CrossRef]
5. Almeida, R.S.M.; Chen, S.A.; Besser, B.; Tushtev, K.; Li, Y.; Rezwan, K. Fatigue behavior and damage analysis of PIP C/SiC composite. *J. Eur. Ceram. Soc.* **2022**, *42*, 5391–5398. [CrossRef]
6. Gao, J.; Zhu, P.; Yuan, Y.; Wu, Z.; Xu, R. Strength and stiffness degradation modeling and fatigue life prediction of composite materials based on a unified fatigue damage model. *Eng. Fail. Anal.* **2022**, *137*, 106290. [CrossRef]
7. Xu, Y.; Zhang, H.; Yang, F.; Tong, L.; Yan, D.; Yang, Y.; Wang, Y.; Wu, Y. Experimental investigation of pneumatic motor for transport application. *Renew. Energy* **2021**, *179*, 517–527. [CrossRef]
8. Wang, X.; Lyu, X. Experimental study on vertical water entry of twin spheres side-by-side. *Ocean. Eng.* **2021**, *221*, 108508. [CrossRef]
9. Xiong, X.; Ma, Q.; Yingying, Y.; Wu, Z.; Zhang, M. Current situation and key manufacturing considerations of green furniture in China: A review. *J. Clean. Prod.* **2020**, *267*, 121957. [CrossRef]
10. Watkins, M.; Casamayor, J.L.; Ramirez, M.; Moreno, M.; Faludi, J.; Pigosso, D.C.A. Sustainable Product Design Education: Current Practice. *She Ji J. Des. Econ. Innov.* **2021**, *7*, 611–637. [CrossRef]

11. Wang, N.; Wang, H.; Ren, J.; Gao, G.; Zhao, G.; Yang, Y.; Wang, J. High-efficient and environmental-friendly PTFE@SiO_2 core-shell additive with excellent AW/EP properties in PAO_6. *Tribol. Int.* **2021**, *158*, 106930. [CrossRef]
12. Sharma, R.; Jha, B.K.; Pahuja, V.; Sharma, S. Role of environmental friendly machining on machinability. *Mater. Today Proc.* **2022**, *50*, 640–648. [CrossRef]
13. Anselma, P.G. Electrified powertrain sizing for vehicle fleets of car makers considering total ownership costs and CO_2 emission legislation scenarios. *Appl. Energy* **2022**, *314*, 118902. [CrossRef]
14. Barkh, H.; Yu, A.; Friend, D.; Shani, P.; Tu, Q.; Swei, O. Vehicle fleet electrification and its effects on the global warming potential of highway pavements in the United States. *Resour. Conserv. Recycl.* **2022**, *185*, 106440. [CrossRef]
15. Liu, Z.; Guo, Z.; Rao, X.; Xu, Y.; Sheng, C.; Yuan, C. A comprehensive review on the material performance affected by gaseous alternative fuels in internal combustion engines. *Eng. Fail. Anal.* **2022**, *139*, 106507. [CrossRef]
16. Woydt, M. The importance of tribology for reducing CO_2 emissions and for sustainability. *Wear* **2021**, *474*, 203768. [CrossRef]
17. Woydt, M. Material efficiency through wear protection—The contribution of tribology for reducing CO_2 emissions. *Wear* **2022**, *488*, 204134. [CrossRef]
18. Ganesarajan, D.; Simon, L.; Tamrakar, S.; Kiziltas, A.; Mielewski, D.; Behabtu, N.; Lenges, C. Hybrid composites with engineered polysaccharides for automotive lightweight. *Compos. Part C Open Access* **2022**, *7*, 100222. [CrossRef]
19. Junk, S.; Rothe, N. Lightweight design of automotive components using generative design with fiber-reinforced additive manufacturing. *Procedia CIRP* **2022**, *109*, 119–124. [CrossRef]
20. Mistry, P.J.; Johnson, M.S.; Li, S.; Bruni, S.; Bernasconi, A. Parametric sizing study for the design of a lightweight composite railway axle. *Compos. Struct.* **2021**, *267*, 113851. [CrossRef]
21. Solazzi, L. Feasibility study of hydraulic cylinder subject to high pressure made of aluminum alloy and composite material. *Compos. Struct.* **2019**, *209*, 739–746. [CrossRef]
22. Solazzi, L.; Assi, A.; Ceresoli, F. Excavator arms: Numerical, experimental and new concept design. *Compos. Struct.* **2019**, *217*, 60–74. [CrossRef]
23. Collotta, M.; Solazzi, L. New design concept of a tank made of plastic material for firefighting vehicle. *Int. J. Automot. Mech. Eng.* **2017**, *14*, 4603–4615. [CrossRef]
24. Solazzi, L.; Assi, A.; Ceresoli, F. New Design Concept for an Excavator Arms by Using Composite Material. *Appl. Compos. Mater.* **2018**, *25*, 601–617. [CrossRef]
25. Solazzi, L. Experimental and analytical study on elevating working platform. *Procedia Eng.* **2017**, *199*, 2597–2602. [CrossRef]
26. Solazzi, L. Design and experimental tests on hydraulic actuator made of composite material. *Compos. Struct.* **2020**, *232*, 111544. [CrossRef]
27. Solazzi, L.; Buffoli, A. Telescopic Hydraulic Cylinder Made of Composite Material. *Appl. Compos. Mater.* **2019**, *26*, 1189–1206. [CrossRef]
28. Solazzi, L.; Buffoli, A. Fatigue design of hydraulic cylinder made of composite material. *Compos. Struct.* **2021**, *277*, 114647. [CrossRef]
29. Huang, W.; Zhong, H.; Lei, L.; Fang, G. Microstructure and mechanical properties of multi-pass forged and annealed 42CrMo steel. *Mater. Sci. Eng. A* **2022**, *831*, 142191. [CrossRef]
30. Kali, N.; Chelimilla, N.; Korla, S. Influence of damages (hole/slits) on tensile behavior of Al 7075-T6/glass fibre-based hybrid laminates. *Mater. Today Proc.* **2022**, *56*, 631–636. [CrossRef]
31. Puttaraju, D.G.; Hanumantharaju, H.G. Finite element analysis and validation of tensile properties of carbon fiber reinforced polymer matrix composites. *Mater. Today Proc.* **2022**, *62*, 2800–2807. [CrossRef]
32. Abdollahzadeh, M.A.; Ali, H.Q.; Yildiz, M.; Kefal, A. Experimental and numerical investigation on large deformation reconstruction of thin laminated composite structures using inverse finite element method. *Thin-Walled Struct.* **2022**, *178*, 109485. [CrossRef]
33. Yan, B.; Zhu, S.; Tong, M.; Pan, S. Experimental study on the mechanical properties of laminates made of thin carbon fiber plies. *Compos. Struct.* **2020**, *245*, 112336. [CrossRef]
34. Solazzi, L. Stress variability in multilayer composite hydraulic cylinder. *Compos. Struct.* **2021**, *259*, 113249. [CrossRef]
35. Buragohain, M.K. *Composite Structures: Design, Mechanics, Analysis, Manufacturing, and Testing*; CRC Press: Boca Raton, FL, USA, 2017.
36. Gay, D.; Hoa, S.V. *Composite Materials. Design and Applications*, 3rd ed.; CRC Press: Boca Raton, FL, USA, 2015; pp. 118–119.
37. Bedi, D.; Sharma, S. Prediction of principal stresses and strains in laminated composites using MATLAB. *Mater. Today Proc.* **2021**, *44*, 4643–4650. [CrossRef]
38. Singh, J.; Kumar, A.; Szafraniec, M.; Barnat-Hunek, D.; Sadowska-Buraczewska, B. Static Analysis of Skew Functionally Graded Plate Using Novel Shear Deformation Theory. *Materials* **2022**, *15*, 4633. [CrossRef]
39. Mognhod Bezzie, Y.; Paramasivam, V.; Tilahun, S.; Selvaraj, S.K. A review on failure mechanisms and analysis of multidirectional laminates. *Mater. Today Proc.* **2021**, *46*, 7380–7388. [CrossRef]
40. Mishra, B.B.; Kumar, A.; Zaburko, J.; Sadowska-Buraczewska, B.; Barnat-Hunek, D. Dynamic Response of Angle Ply Laminates with Uncertainties Using MARS, ANN-PSO, GPR and ANFIS. *Materials* **2021**, *14*, 395. [CrossRef]
41. Balasubramanian, M. *Composite Materials and Processing*; CRC Press: Boca Raton, FL, USA, 2013.
42. Kar, K.K. *Composite Materials: Processing, Applications, Characterizations*; Springer: Cham, Switzerland, 2016.

43. Azeem, M.; Ya, H.H.; Alam, M.A.; Kumar, M.; Stabla, P.; Smolnicki, M.; Gemi, L.; Khan, R.; Ahmed, T.; Ma, Q.; et al. Application of Filament Winding Technology in Composite Pressure Vessels and Challenges: A Review. *J. Energy Storage* **2022**, *49*, 103468. [CrossRef]
44. Tiwari, A.; Alenezi, M.R.; Jun, S.C. *Advanced Composite Materials*; Composite Materials for Application in Printed Electronics; Scrivener Publishing LLC.: Beverly, MA, USA, 2016.
45. Vassilopoulos, A.P. *Fatigue and Fracture of Adhesively-Bonded Composite Joints*; Woodhead Publishing: Sawston, UK, 2015; pp. 443–491.
46. Barbosa, J.F.; Correia, J.A.; Júnior, R.F.; Zhu, S.P.; Jesus, A.M.D. Probabilistic S-N fields based on statistical distributions applied to metallic and composite materials: State of the art. *Adv. Mech. Eng.* **2019**, *11*, 168781401987039. [CrossRef]
47. Köbler, J.; Magino, N.; Andrä, H.; Welschinger, F.; Müller, R.; Schneider, M. A computational multi-scale model for the stiffness degradation of short-fiber reinforced plastics subjected to fatigue loading. *Comput. Methods Appl. Mech. Eng.* **2021**, *373*, 113522. [CrossRef]
48. Murakami, Y.; Takagi, T.; Wada, K.; Matsunaga, H. Essential structure of S-N curve: Prediction of fatigue life and fatigue limit of defective materials and nature of scatter. *Int. J. Fatigue* **2021**, *146*, 106138. [CrossRef]
49. Muc, A. Fuzzy approach in modeling static and fatigue strength of composite materials and structures. *Neurocomputing* **2020**, *393*, 156–164. [CrossRef]
50. Vassilopoulos, A.P.; Maier, J.; Pinter, G.; Gaier, C. 18—Computational tools for the fatigue life modeling and prediction of composite materials and structures. In *Fatigue Life Prediction of Composites and Composite Structures*, 2nd ed.; Vassilopoulos, A.P., Ed.; Woodhead Publishing: Sawston, UK, 2020; pp. 635–680.
51. Maljaars, J.; Leonetti, D.; Hashemi, B.; Snijder, H.H. Systematic derivation of safety factors for the fatigue design of steel bridges. *Struct. Saf.* **2022**, *97*, 102229. [CrossRef]
52. Huang, Z.; Ma, W.; Jia, C.; Lei, X.; Zhang, Z.; Ma, Z. Gradient design of tubular of the fiber-reinforced composites pressure vessel for diminishing of the edge effect. *Int. J. Press. Vessel. Pip.* **2021**, *192*, 104398. [CrossRef]
53. Kushwah, S.; Parekh, S.; Mistry, H.; Darji, J.; Gandhi, R. Analysis of cylindrical pressure vessels with dissimilar ends and material comparison. *Mater. Today Proc.* **2022**, *51*, 355–368. [CrossRef]
54. Wu, E.; Zhao, Y.; Zhao, B.; Xu, W. Fatigue life prediction and verification of high-pressure hydrogen storage vessel. *Int. J. Hydrogren Energy* **2021**, *46*, 30412–30422. [CrossRef]
55. Cardoso, A.S.M.; Pardal, J.M.; Chales, R.; Martins, C.H.; Silva, M.M.; Tavares, S.S.M.; Pedroza, B.C.; Barbosa, C. Fatigue resistance performance of universal cardan joint for automotive application. *Eng. Fail. Anal.* **2022**, *135*, 106128. [CrossRef]
56. Balavignesh, V.N.; Balasubramaniam, B.; Kotkunde, N. Numerical investigations of fracture parameters for a cracked hydraulic cylinder barrel and its redesign. *Mater. Today Proc.* **2017**, *4*, 927–936. [CrossRef]